28 GHz Wireless Backhaul Transceiver Characterization and Radio Link Budget

Marko E. Leinonen, Giuseppe Destino, Olli Kursu, Marko Sonkki, and Aarno Pärssinen

Millimeter wave communication is one of the main disruptive technologies in upcoming 5G mobile networks. One of the first candidate applications, which will be commercially ready by 2020, is wireless backhaul links or wireless last mile communication. This paper provides an analysis of this use-case from radio engineering and implementation perspectives. Furthermore, preliminary experimental results are shown for a proof-of-concept wireless backhaul solution developed within the EU-KR 5GCHAMPION project, which will be showcased during the 2018 Winter Olympic Games in Korea. In this paper, we verify system level calculations and a theoretical link budget analysis with conductive and radiated over-the-air measurements. The results indicate that the implemented radio solution is able to achieve the target key performance indicator, namely, a 2.5 Gbps data rate on average, over a range of up to 200 m.

Keywords: Antenna array, Antenna pattern, Array receiver, Millimeter wave radio, Noise figure, Radio link budget.

I. Introduction

One of the key drivers for the development of the next generation of communication systems, that is, 5G, is the demand for communication data rates that are 10 times higher than the current long term evolution (LTE; 20 Gbps and 10 Gbps peak rates for downlink and uplink, respectively). A promising and concrete approach is to exploit the large amount of available spectrum in the K_a–band (26.5 GHz–40 GHz) [1] to allow the transmission of wide-band signals (from 100 MHz to 1 GHz bandwidth). However, this necessitates the usage of large antenna arrays with adaptive beamforming capabilities to combat the path loss and sensitivity of the radio links to dynamic obstructions. In [2], for instance, the results of a channel measurement campaign at 28 GHz[1)] show how the line-of-sight and multipath components of the radio channel are highly affected by moving objects such as cars.

In the literature as well as prototype demonstrations, only a few implementations of 28 GHz transceivers have been proposed. For instance, in [3], a 28 GHz CMOS direct conversion transceiver with eight antennas integrated in the same package was proposed. However, the transmission power is limited because the saturated output power (Psat) of a single amplifier is 10.5 dBm. This limits the conducted transmission power to 3 dBm with LTE modulation. In [4], a 32-path transceiver was presented with a 16 dBm Psat output power from each path, which results in ~6 dBm conducted modulated signal power with 10 dB peak-to-average ratio.

In this work, the focus is on the design and validation of a radio frequency (RF) transceiver [5] operating in the

Manuscript received Oct. 10, 2017; revised Dec. 4, 2017; accepted Dec. 18, 2017.

Marko E. Leinonen (corresponding author, marko.e.leinonen@oulu.fi), Giuseppe Destino (giuseppe.destino@oulu.fi), Olli Kursu (olli.kursu@oulu.fi), Marko Sonkki (marko.sonkki@oulu.fi), and Aarno Pärssinen (Aarno.Parssinen@oulu.fi) are with Centre for Wireless Communications, University of Oulu, Finland.

[1)] The frequency band at 28 GHz is not allocated for mobile services in Europe. However, due to the strong opening from other countries (US, Korea, and Japan), the European Commission recommends the 24.25 GHz–27.5 GHz as a pioneer band for 5G above 24 GHz.

frequency band of 27.5 GHz−28.5 GHz. This band represents a frequency band partially endorsed in common by the European, Korean, US, and Japanese Frequency Spectrum Authorities, and it is the specification for the 5G trials at the Winter Olympics in Korea [6].

From a design perspective, the proposed RF implementation can be considered one of the first complete solutions capable of achieving millimeter wave (mmW) urban backhaul requirements, that is, medium-long range coverage and robustness to dynamic changes in the environment. In contrast to [3] and [4], which are integrated circuit (IC) solutions, the proposed implementation is able to produce a conductive power of more than 30 dBm. Additionally, our solution can produce 60 dBm effective isotropic radiated power (EIRP), while the IC based transceivers provide 24 dBm EIRP [3] and 28 dBm [4]. In addition, the proposed solution supports higher multiple-input and multiple-output (MIMO) capabilities.

Furthermore, from a validation and experimentation viewpoint, we show how to circumvent the problem of measuring the noise figure of an antenna array receiver. More specifically, we propose a new noise figure measurement method that is based on a modulation accuracy measurement with conducted, or (preferably) over-the-air (OTA) measurement. The OTA based method has some advantages over traditional conductive noise figure measurements when a high number of receiver paths are measured simultaneously.

The conductive measurement setup requires complex cabling, and noise figure measurement requires a narrow measurement bandwidth to improve its accuracy. Additionally, the method is sensitive to receiver gain ripple, and narrow-band signals are not realistic signals for a wideband receiver. The effective isotropic noise figure was recently proposed by [7], where the noise figure is measured with a radiated noise temperature that requires a narrow measurement bandwidth. Our proposed method is based on a digitally modulated wideband OTA test signal. The received signal is demodulated and the noise figure is derived from the error vector magnitude (EVM) of the received signal.

The paper is organized as follows. Section II presents an overview of the radio architecture and presents the design principles of mobile backhaul radio, including assumptions with initial radio link budget calculations. Section III focuses on the design and characterization of the implemented antenna array. Section IV presents the quantitative results of for the noise figure of the receiver beam former, and Section V presents the resulting link budget analysis, which includes realistic measured radio performance figures. Finally, in Section VI, the conclusions are drawn and remarks are made.

II. Design Requirements and Radio Architecture of Wireless Backhaul System

The proposed mmW wireless backhaul system has been designed to meet the following requirements [8]: (i) long coverage (a few hundreds of meters), (ii) over 2 Gbps data rate, (iii) MIMO transmissions, and (iv) adaptive beamforming. We employ large antenna arrays to improve coverage, RF beam steering, beam broadening abilities for beam adaptation, and orthogonal frequency division multiplexing (MIMO-OFDM), and high-order modulation to achieve the desired data rate. Details on the actual implementation architecture, system specifications [9], and baseband configurations [10] are provided in Fig. 1, Tables 1 and 2, respectively.

From an RF architecture viewpoint, Fig. 1 shows that four antenna arrays are utilized for the transmission of eight digital streams. This clearly indicates that, in pairs, streams are aggregated in the RF domain and, subsequently, the antenna and RF components need to support wideband signals.

In addition, Table 2 shows that the target data rate can be achieved with different configurations and, in particular, with different numbers of streams. Because the baseband is capable of 8 × 8 MIMO, carrier component aggregation is also required and, the lower the modulation, the larger the number of carrier components that need to be aggregated.

A radio link budget based on the aforementioned requirements and system design parameters are presented in Table 3. This radio link budget is based on the theoretical assumptions that the receiver has maximum

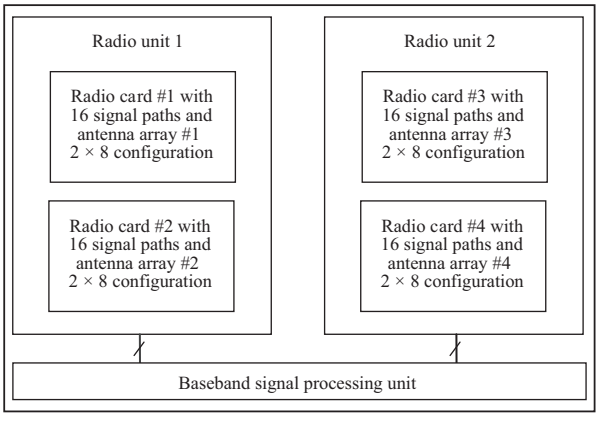

Fig. 1. Block diagram of the full unit supporting 4 × 4 MIMO transmission and reception.

https://doi.org/10.4218/etrij.2017-0231

Table 1. Summary of system design targets for different technology areas of proof-of-concept millimeter wave radio solutions.

Main radio technology areas		
Antenna	Radio solution	Baseband
Phased-array (16 × 4 radiators) with/without antenna transmit array	26.5 GHz–29.3 GHz	Wideband 1 GHz signal bandwidth
Structure 8 × 2 RF beamformer – with 2 × 2 antenna subarray in each, linearly polarized	Operational band at the Olympics: 26.5 GHz–27.5 GHz	8 × 8 MIMO-OFDM (symmetric in uplink and downlink)
Maximum gain 22.7 dBi (sim.), full array	4 RF beam formers (phase shift based)	Max bandwidth: 8 × 100 MHz carrier components
N/A	Digital phase shift control, branch enabled, gain control	Modulation up to 64-QAM (quadrature amplitude modulation)

Table 2. Stream and modulation requirements to achieve the (average) target rate of 2.5 Gbps.

Baseband performance				
Modulation	4-QAM (QPSK)	16-QAM	64-QAM	256-QAM
Fast fourier transform size	2,048	2,048	2,048	2,048
Channel bandwidth (MHz)	100	100	100	100
Subcarrier spacing (kHz)	75	75	75	75
Modulation	4	16	64	256
Coding rate	0.85	0.85	0.85	0.85
UL/DL ratio (%)	50	50	50	50
Achievable-rate per stream (Gbps)	0.08	0.16	0.24	0.32
Number of streams	32	16	11	8
Target rate (Gbps)	2.5	2.5	2.5	2.5

coherence gain, both transmission and reception antenna arrays provide the maximum theoretical antenna gain, the radio front end is implemented with a bandpass preselection filter, the transmission power is 30 dBm, and the noise figure of the receiver is 10 dB.

All these assumptions are addressed in other sections in the paper. In Section V, a revised link budget is presented.

Table 3. Link budget calculation based on 64-QAM modulation and 100 MHz channel bandwidth at 27.0 GHz.

	Parameter	Value	Unit
A	Number of antenna elements or antenna array gain	16	N/A
		12.04	dB
B	Gain of antenna element	10.72	dB
C	SNRmin	25.20	dB
D	SNRmin_coded	24.49	dB
E	Transmitter (TX) EVM	−26.00	dB
F	RX SNR Requirement (D – E on linear scale)	29.83	dB
G	Noise density	−174.00	dBm/Hz
H	Thermal noise power over channel	−94.17	dBm
I	Receiver (RX) noise figure	10.00	dB
J	Sensitivity of one receiver (F + H + I)	−54.35	dBm
K	Conducted transmission power of each transmission path	30.00	dBm
L	Antenna gain transmitter (A + B)	22.76	dBi
M	Antenna gain receiver (A + B)	22.76	dBi
N	TX front end losses	5.00	dB
O	EIRP (K + A – N + L)	59.76	dBm
P	Link margin (O – J + M)	136.87	dB
Q	Path loss coefficient	2.50	N/A
R	Wavelength	11.1	mm
S	Maximum distance	263.58	m

III. Design of Receiver and Transmitter Radio Solution

In this section, we focus on a description and analysis of the implemented mmW radio transceiver [5], which is designed for a time-division-duplex communication, where the transmitting and receiving paths are not simultaneously utilized, but separated by an RF switch.

The beamforming functionality of the radio solution is implemented at RF with digitally controlled phase shifters but without amplitude control. This is because amplitude control of each transmission and reception signal path would require a dedicated gain control component, resulting in a complex circuit board design and calibration control. The phase shifters are controlled by RF beamformer logic and are used to modify the signal phase at the input (or output) of each of the antenna elements. The same phase shifters are used for the transmission and reception of the signals. A signal distribution network that combines and splits the RF signal is common for both transmission and reception. A three-stage cascade of the

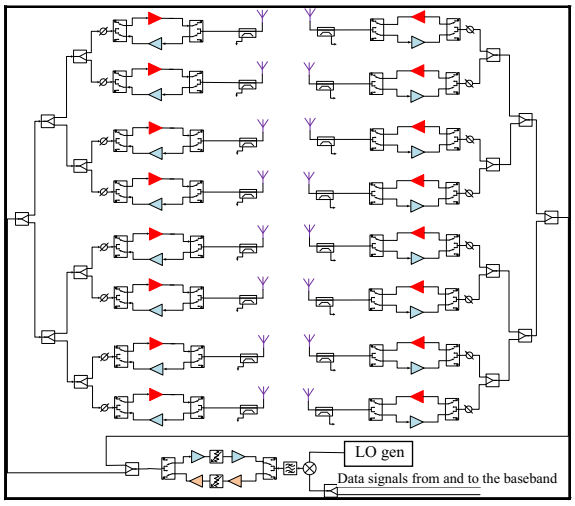

Fig. 2. Block diagram of the proof-of-concept radio unit supporting two 2 × 8 antenna element arrays.

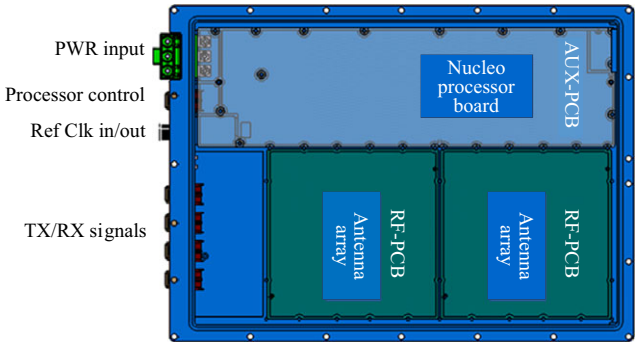

Fig. 3. Mechanical overview of the radio unit [9].

power-splitting network is used to minimize network insertion losses when one side of the radio card supports eight antenna elements. A block diagram of the radio card is shown in Fig. 2, and a mechanical overview of the structure of one radio unit is presented in Fig. 3 with two integrated radio cards [9]. A mixer is used to upconvert or downconvert the RF signal to an intermediate frequency (IF) that is used by the digital front end.

1. Radio System Design of Transmitter and Receiver

On the transmit path, the signal is up-converted from the 1 GHz−6 GHz IF frequency to the final transmission frequency of 26 GHz−30 GHz using a commercial subharmonically pumped 21 GHz–31 GHz GaAs mixer with an integrated local oscillator LO-amplifier.

Subharmonic pumping alleviates the requirement for the LO-generation because the final RF-frequency is 2 × LO + IF, which means that the synthesizer can

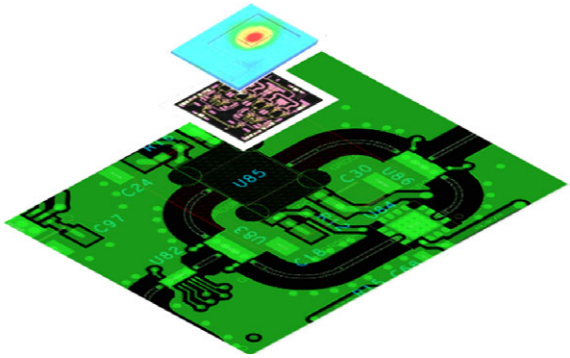

Fig. 4. Thermal simulation of the PA.

operate at less than half of the final frequency. A three-stage Wilkinson power divider network is used to divide the signal to eight antenna modules. Finally, the signal is amplified before the power divider network using two gallium nitrate (GaN) power amplifiers (PAs). Each antenna branch contains a digitally controlled passive phase shifter that can be controlled with 11.25° steps.

The last stage of power amplification is done with a GaN-based PA, namely the TGA2595 [11]. This specific amplifier can provide up to 30 dB gain, its output third-order intercept point is 48.5 dB, and its power added efficiency (PAE) is 24%. However, when using higher order QAM schemes, 10 dB or more backoff is required to achieve the required EVM which reduces the PAE significantly.

In this system, special attention is paid to the heat dissipation of the PA. In fact, the thermal plot shown in Fig. 4 indicates that high temperatures can be reached in the operational mode. The implemented solution is to solder each PA on a Cu coin that perforates the printed wire board (PCB) material and is directly attached to a heat sink on the bottom side of the PCB.

In the receiver path, one of the most important components is the first low noise amplifier (LNA). Here, we used a gallium arsenide (GaAs) monolithic microwave integrated circuit operating on the 22 GHz–38 GHz band. The LNA has a noise figure of 2.5 dB and a gain of 19 dB.

Receiver gain is controlled by a digital attenuator with 5-bit resolution that is located between the two LNAs following the power-combining network. The receiver path contains a commercial logarithmic power detection circuit that acts as a received signal strength indicator for the combined output.

2. Radio Control Software

As illustrated in Fig. 3, each radio unit contains an auxiliary (digital) module for a microcontroller unit. The reason is to perform RF calibrations, beamforming and

https://doi.org/10.4218/etrij.2017-0231

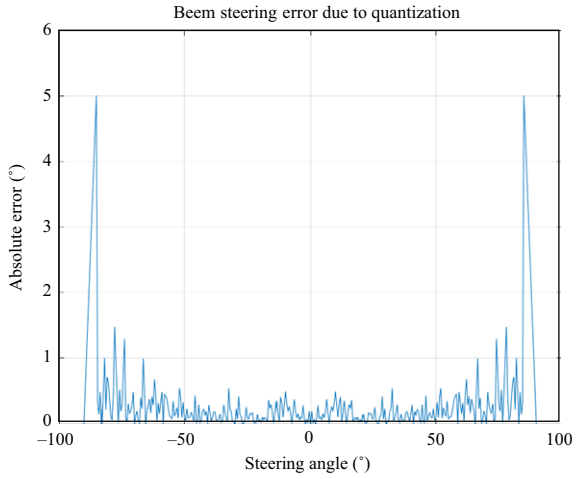

Fig. 5. Effect of phase shifter resolution to beam steering accuracy.

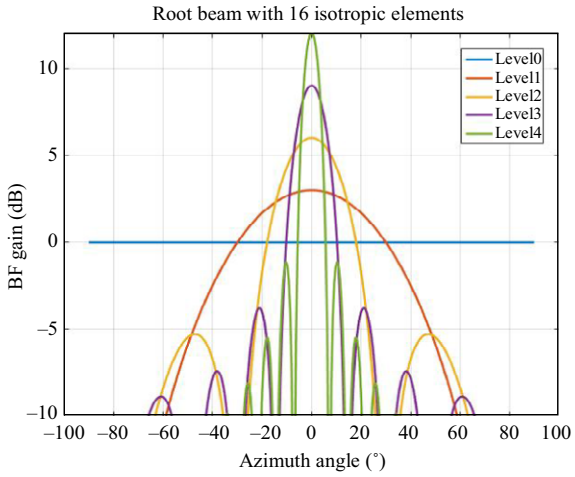

Fig. 7. SubArray. Example of multi-level beampattern using subarray broadening and antenna deactivation.

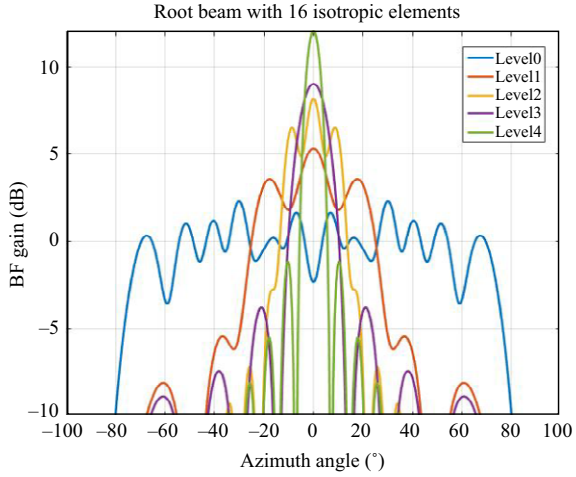

Fig. 6. DEACT. Example of a multilevel beam pattern using only antenna deactivation.

beam alignment procedures thus easing the need for control signaling to the baseband.

The effect of the finite resolution of phase shifter was simulated, and the result is shown in Fig. 5. The mean error of beam steering is 0.229° between −84° to 84°, when a step size of 0.5° is used in the simulation. The quantized result is 90° between 84° and 90° and −84° and −90°, leading to a 5° error. Phase calibration between radio paths is implemented with a look-up table based on measurement results for the phase shifter control words.

Figures 6 and 7 show two types of multilevel beam patterns supported by the implemented mmW transceiver. The first one is based on antenna element deactivation and provides beams with relatively high sidelobes but a smooth beam shape. The second one is based on the subarray broadening deactivation technique proposed in [12]. In contrast to the deactivation approach, this method provides lower sidelobes and maximum emission power, but it has a beam shape with ripples. In addition, as shown in [12], it also improves the probability of beam alignment under many channel propagation conditions.

The measured raise time of the phase shifter is 30 ns and the raise time of the RF switch is 20 ns; thus, they do not limit the speed of beam alignment. The beam alignment procedure has not been fully implemented at the time of writing.

IV. Implemented Antenna Array Solution with Measurement Results

In Fig. 8, a prototype antenna with a 2 × 8 antenna matrix is shown. The array consists of 16 sub-arrays which each include a 2 × 2 patch antenna element, oriented in

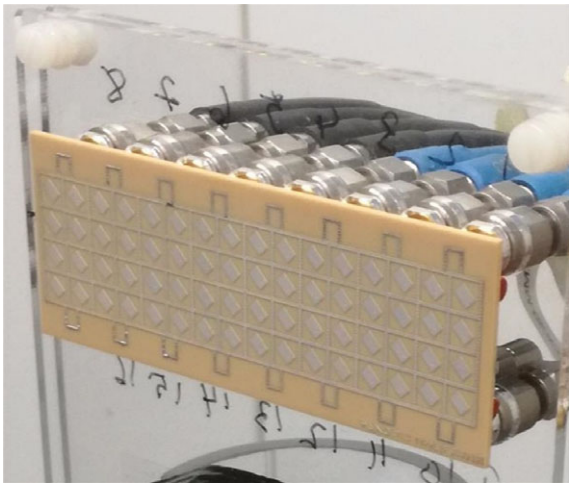

Fig. 8. Photograph of a 2 × 8 sub-array antenna prototype with measurement cables connected to the antenna connectors.

−45° polarization. Thus, the total number of elements in the array matrix is 64, and the size of the array is 90 × 34 mm^2 ($W \times L$). The physical dimensions of a single sub-array are 10.7 × 10.7 × 1.6 mm^3 ($L \times W \times H$), and the size of the sub-array was driven by the sizes of the radio components available on the open market. The structure includes RF connectors called SMPM and a metal cover over the feed network to prevent backward radiation. The total form-factor of the planar antenna array is 9.6 × 2.4 cm^2. The presented radiation pattern simulation and measurement results are based on the first version of the antenna array, where the goal of −10 dB impedance bandwidth was set for 26.65 GHz to 27.50 GHz. The target for the second version of the antenna array is to fulfill the bandwidth from 24.25 GHz to 29.20 GHz, and it will present two orthogonal polarizations components (±45°).

In Fig. 9, simulated and OTA measured beam patterns of the full 2 × 8 antenna matrix are presented. The azimuth plane (horizontal plane) results are shown because the horizontal direction is emphasized more than the elevation, as the beams are narrower in the azimuth plane. The radiation patterns are measured element by element and the results are summed in postprocessing. The side lobe levels

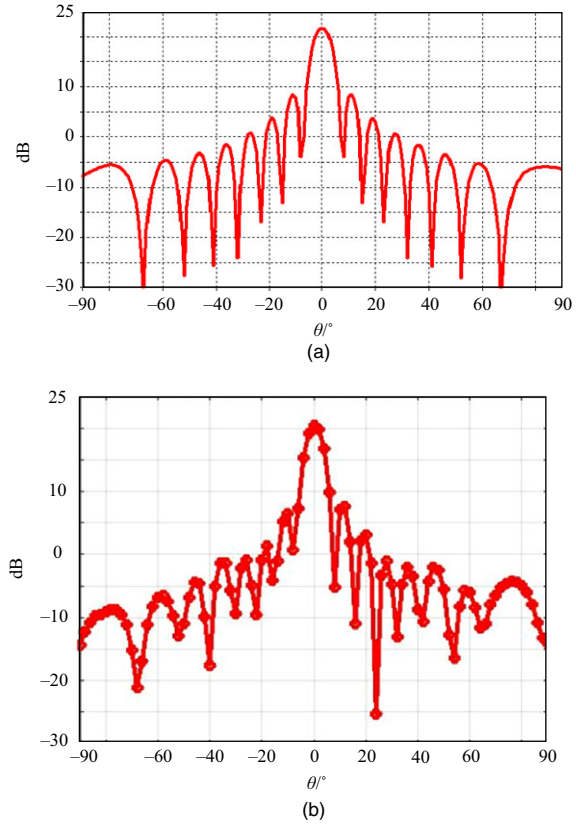

Fig. 9. Radiation patterns of 2 × 8 antenna array matrix: (a) simulated and (b) measured results at 26.5 GHz in the azimuth plane.

of the antenna array are 15 dB below the maximum gain, which agrees well with simulation results. The measured maximum gain of the antenna array is approximately 20 dBi, which is close to the simulated value of 21.5 dBi.

The following OTA measurements for the radio solution were performed with a 1 × 8 antenna array configuration and, thus, the maximum antenna gain was reduced by 3 dBs to 17 dBi.

V. Quantification of the Receiver Beamformer Noise Figure

The noise figure of a radio receiver is how much the receiver increases noise above the thermal noise level when a signal passes through it. The noise figure of the receiver limits the level of signal that can be received. Thus, measuring the noise figure is one of the most important tasks in radio receiver characterization.

1. System-Level Calculation of the Receiver Array Noise Figure

The noise figure for any receiver can be defined using the signal-to-noise (SNR) ratios of the input and output of the receiver

$$SNR_{\text{output}} = SNR_{\text{input}} - NF, \quad (1)$$

where SNR_{output} is the SNR in the output of the receiver, SNR_{input} is the SNR in the input of the receiver, and NF is the noise figure of the receiver (all expressed in dB).

The noise figure for a phased array receiver is more complicated to define than for a single path because it depends on the definition of the input signal-to-noise ratio. One approach is to analyze the antenna array as a single path receiver if the first LNA has high enough gain [13]. Multiple receiver paths can improve the SNR of the received signal. In a phased array receiver, the received signals from the antenna array elements are rotated into the same phase to facilitate coherent signal combination. This is equivalent to steering the combined antenna pattern to the direction of the incoming signal. Noise from antenna elements has a random phase, which means that the noise is combined incoherently. That is, it is combined as root mean square power. The SNR of an array receiver can be ideally improved by N times or $10 \cdot \log_{10}(N)$ dB with respect to single-receiver SNR, where N is the number of receiver paths. This gain is referred to as the coherence gain. A high number of receiving antennas in the array could mathematically lead to a situation where the calculated noise figure of the receiver is negative on logarithm scale, which is not physically feasible [14]. This

https://doi.org/10.4218/etrij.2017-0231

is compensated for by a correction factor that keeps the noise figure above zero [14].

In practical implementations, the coherence gain will be lower than the theoretical value because of component variations like IC manufacturing and packaging process variations. In addition, the layout has an impact on the radio performance because, in practice, it is not possible to make the signal lines perfectly similar and the layout will not be perfectly symmetrical.

If the gain of an individual receiver path N is denoted by G_N and the input power conducted into the receiver path from antenna element N is P_{in}, then the combined output signal in the output of receiver P_{out} is

$$P_{\text{out}} = P_{\text{in}}(G_1 + G_2 + \cdots + G_N). \tag{2}$$

If all receiver paths have equal gains $G_1 = G_2 = G_N$, then the output is

$$P_{\text{out}} = P_{\text{in}}(G_1 + G_1 + \cdots + G_1) = P_{\text{in}}G_1N, \tag{3}$$

where N is the number of receiver paths. If the receiver paths have unequal gains and G_1 is the maximum gain, then the output is

$$\begin{aligned} P_{\text{out}} &= P_{\text{in}}G_1(1 + G_2/G_1 + \cdots + G_N/G_1) \\ &= P_{\text{in}}G_1 \sum_{k=1}^{N}(1 + G_k/G_1) < P_{\text{in}}G_1N. \end{aligned} \tag{4}$$

Hence, the coherence gain achievable with unequal gains is lower than that with equal gains depending on the gain ratios. Similarly, with OTA measurements, if the antenna elements in the array have unequal antenna gains, the power conducted from the antenna follows (4). In the OTA case, P_{in} is the radiated input signal level and G_k is the antenna gain of the antenna element.

If one or more antennas or receiver paths have higher gains than the others, then the available coherence gain may be reduced significantly.

An RF system-level analysis of the cascaded noise figure and cascaded gain of the implemented radio solution is shown in Fig. 10 [5]. The noise figure calculated for the receiver array with eight receiver paths is 8.0 dB, and the noise figure for one receiver path is 21.0 dB. An image of the radio solution is shown in Fig 11, which is half of the final radio board implementation, as shown in Fig. 2.

2. Measurement of the Receiver Array Noise Figure

The noise figure of a receiver can be measured in different ways, and one conductive measurement method is to feed a signal with a known SNR into an input of the receiver and measure the SNR at the output of the receiver. The two signals are then compared. Another conductive measurement method is based on measuring the gain of a receiver with a continuous wave (CW) signal. After the gain measurement, the thermal noise level at the output of the receiver is measured when the input is terminated with a 50 Ω standard load. The noise level is measured with a narrow measurement bandwidth to increase the sensitivity of the measurement. This method is shown in Figs. 12(a) and (b).

A block diagram of the measurement system for the proposed OTA noise figure measurement based on signal quality is shown in Fig. 12(c). A test signal is transmitted OTA, the received signal is demodulated, and the noise figure is calculated from the received signal EVM or SNR.

The modulated signal that is used in the OTA noise figure measurement is a standard digital wideband

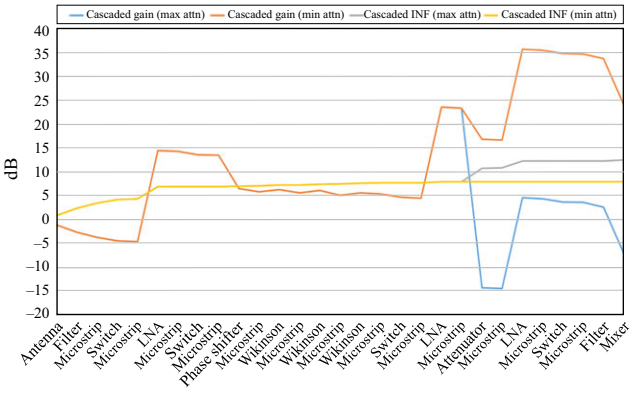

Fig. 10. Cascaded signal level and linearity block level analyses for 8 receiver paths [5].

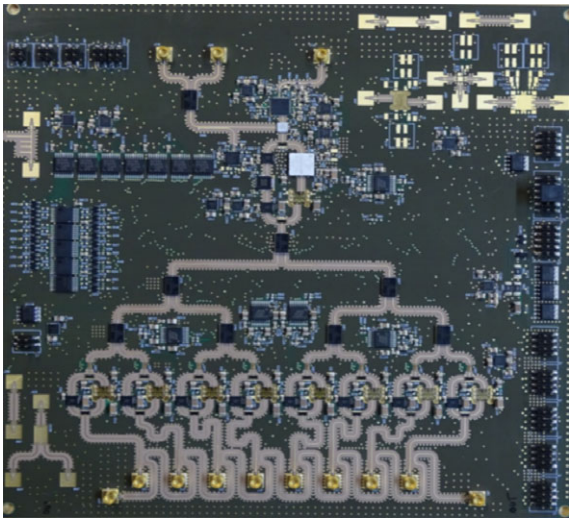

Fig. 11. Image of the proof-of-concept 28-GHz band radio transceiver board supporting an 1 × 8 antenna array [5].

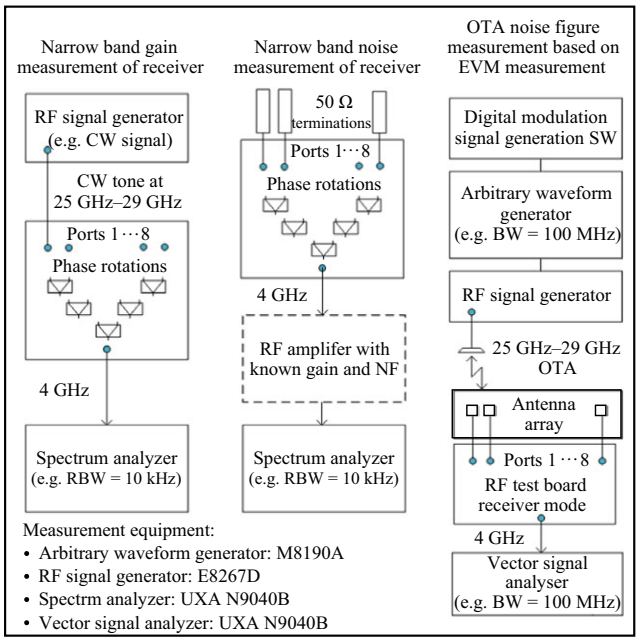

Fig. 12. Noise figure measurement system configurations for (a) CW gain measurement, (b) thermal noise measurement, and (c) radiated modulated signal.

modulated signal, which is transmitted via a known reference antenna to the antenna array receiver. Photographs of the OTA measurement setups are shown in Figs. 13(a) and (b). The measured antenna array is placed in front of the absorber material and the measured radio unit is behind the absorber. This arrangement prevents coupling of the OTA signal directly with the radio receiver signal paths. OTA measurements were performed at a 2-m distance, which is the far-field region of the receiving antenna array.

Fig. 13. Measurement setups: (a) modulated signal measurement system with reference antenna and (b) EVM OTA measurement with line-of-sight.

The received output signal level $Pout_{\mathrm{RX}}$ in the OTA measurement is measured directly from the output of the receiver and can be calculated as follows.

$$Pout_{\mathrm{RX}} = P_{\mathrm{TX}} - IL_{\mathrm{TX}} + Gant_{\mathrm{TX}} - IL_{\mathrm{path}} + \sum_{i=1}^{N} Gant_i^{\mathrm{RX}} - IL_i^{\mathrm{RX}} + Gpath_i^{\mathrm{RX}}, \quad (5)$$

where P_{TX} is the transmission power of the test signal, IL_{TX} is the cable loss between the signal generator and the transmission antenna, $Gant_{\mathrm{TX}}$ is the transmission antenna directivity and radiation efficiency, IL_{path} is the free space loss of the signal at the test frequency, $Gant_i^{\mathrm{RX}}$ is the antenna directivity and radiation efficiency of antenna i, IL_i^{RX} is the cable loss between the antenna and receiver path i and $Gpath_i^{\mathrm{RX}}$ is the power gain of receiver i with the modulated wideband test signal.

The modulation accuracy of the received signal is measured with a modulation analyzer, which can measure the output power level and EVM. EVM is a metric of digital modulation accuracy, and it depends on the SNR of a signal. EVM can be defined for both received and transmitted signals, and radio system specifications state the requirements for the transmission EVM levels. EVM is defined according to the following equation [15].

$$EVM = \frac{\sqrt{\frac{1}{N}\sum_{n=0}^{N-1} I_{\mathrm{err}}[n]^2 + Q_{\mathrm{err}}[n]^2}}{P_{\mathrm{reff}}}, \quad (6)$$

where n is a symbol index, N is the number of symbols, $I_{\mathrm{err}} = I_{\mathrm{ref}} - I_{\mathrm{meas}}$ is the error of signal I from the reference point and $Q_{\mathrm{err}} = Q_{\mathrm{ref}} - Q_{\mathrm{meas}}$ is the error of signal Q from the reference point. The EVM has the following direct relationship to the received signal SNR [16]:

$$SNR = Pout_{\mathrm{RX}} - Noise = -20 \cdot \log_{10}\left(\frac{EVM}{100}\%\right). \quad (7)$$

The power gains of the receiver paths of the receiver array with a 16-QAM modulated 100-MHz wide test signal with a 100-MHz step size over the operation frequency range were measured, and the results are shown in Fig. 14. A significant gain ripple of almost 15 dB can be seen over the operational frequency range on all receiver paths. The gain variation among signal paths is caused by component variations, but is mainly due to manufacturing defects of in the wire bonding of the phase shifter components.

The noise figure of the receiver can be calculated at a fixed EVM value by comparing the noise level of the SNR of the EVM measurement to thermal noise level of a modulation bandwidth. More accurate noise figures can be

https://doi.org/10.4218/etrij.2017-0231

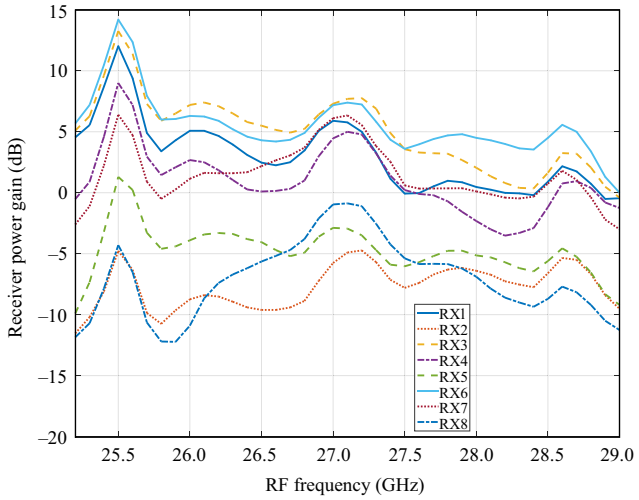

Fig. 14. Small signal gains of receiver paths of the array receiver measured with modulated 100 MHz test signal with OTA.

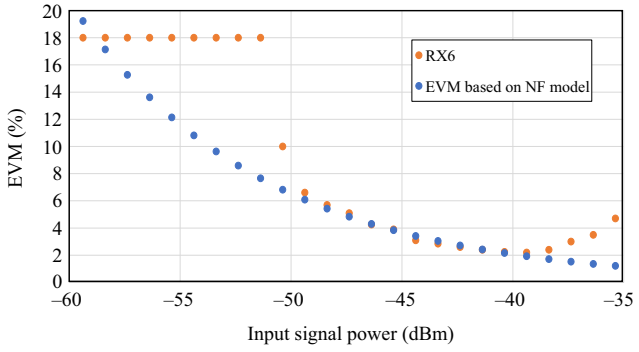

Fig. 15. Noise figure modeling using MSE in the noise-limited EVM region.

calculated by curve fitting the EVM measurement results with an EVM curve with varying SNR values, which can be calculated from (7). The noise component of SNR can be calculated as

$$Noise = -174\,\text{dBm/Hz} + 10 \cdot \log_{10}(BW) + NF, \quad (8)$$

where BW is the modulation bandwidth of the test signal in Hz and NF is the noise figure of the receiver. The noise figure can be calculated using (6), (7), and (8) when the EVM is measured as a function of the output power of the receiver. A theoretical EVM curve with a known NF can be calculated in a similar manner. The noise figure of the receiver array can be calculated by minimizing the mean squared error (MSE) between the EVM measurement results and the calculated theoretical EVM curve. The noise figure of the receiver is given by the best fit of the EVM curves.

EVM curve fitting for the measurement results and noise figure modeling was performed around the 10-dB signal

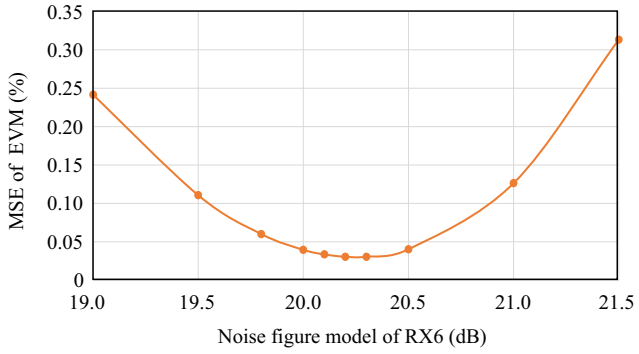

Fig. 16. Best fit of the noise figure model for receiver path 6.

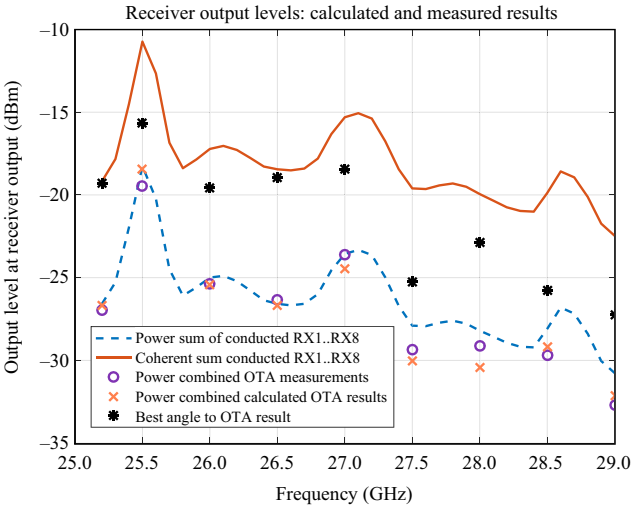

Fig. 17. Measured and calculated RF output signal levels with an eight-receiver path array.

range in the noise-limited signal region. In the noise-limited region of EVM curve, the noise level or noise figure of the receiver is the main contributor to EVM performance. Other EVM contributors such as the gain ripple at the measurement band, LO-phase noise, and carrier leakage are designed to be the main EVM contributors at higher signal levels. The noise-limited EVM region of the measured receiver is at signal levels below −40 dBm. An example of curve fitting for measured and theoretical EVM curves for receiver path 6 is shown in Fig. 15, and the MSE of the curve fitting is shown in Fig. 16.

The coherence gain of the receiver was measured using the OTA method with a 100-MHz wide test signal. A common receiver signal path creates a constant noise floor at the output of the receiver and thus the SNR of the received signal can be improved by activating more receiver paths. The calculated output signal levels based on the conducted gain measurements are shown with solid and dotted lines in Fig. 17. The markers in Fig. 17 indicate OTA measurement results, and a good match between the calculated and measured signal levels can be

seen. Phase rotation is applied to the received signal to maximize the output signal level for the best-angle OTA results. The small difference between the measured and calculated output signal levels can be attributed to signal level variation during the OTA measurements. The mean value of the difference at 26.5 GHz is 0.1 dB with a 1.0 dB standard deviation, at a −37.0 dBm average conducted input signal level after each receiving antenna element is used.

The theoretical coherence gain for eight receiver paths with equal gains is indicated by a blue solid line and the maximum available coherence gain based on the measured signal gains of the receiver array is shown by a red dotted line in Fig 18. Black circles indicate the coherence gain when the best OTA phase-rotated signal is compared to the measured power-combined OTA signal levels. Green crosses show the coherence gain if the best phase-rotated OTA results are compared to the calculated power-combined individual signal levels. A good fit between the calculated and measured coherence gains can be seen. The coherence gain of the receiver is reduced when the gain of the receiver peaks. Moreover, the average measured coherence gain over the frequencies is 5.5 dB.

Individual receiver path noise figure measurement results based on different conducted receiver noise measurement methods are shown in Table 4. It can be seen that the single-point EVM value and curve fitting-based noise figure results are almost equal. The narrowband noise figure measurement results deviate from the wideband results because of the ripple seen at the narrowband gain measurements.

Multiple receiver path noise figure measurements are shown in Table 5. Both conducted and OTA-based noise

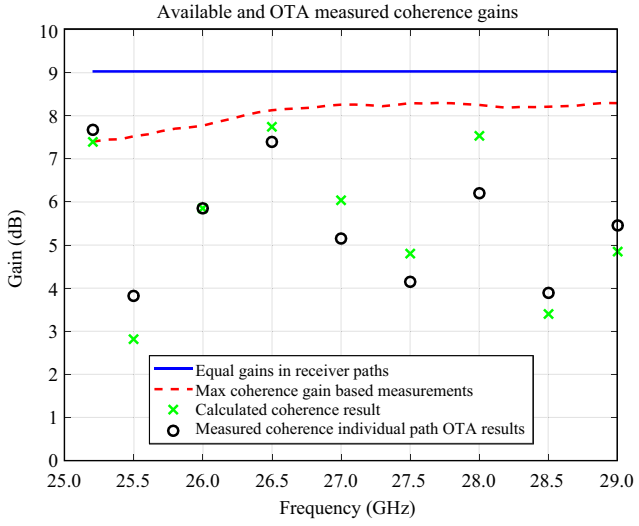

Fig. 18. Measured coherence gains of an eight receiver path array.

Table 4. Conducted noise figures of individual receivers at 26.5 GHz obtained by different measurement methods.

Individual receiver path noise figures (dB)								
Receiver array paths	RX1	RX2	RX3	RX4	RX5	RX6	RX7	RX8
MSE EVM curve fitting	22.5	35.6	20.3	24.8	30.0	21.3	22.1	31.5
Single 4% point EVM result	23.1	36.1	20.1	25.1	30.1	21.0	22.3	31.5
10-kHz noise measurement	16.2	27.8	14.3	17.8	13.4	15.0	16.9	25.5

figure measurement results are shown, and a good match between the OTA and conducted results is seen when two receivers are measured. When two receivers have an almost equal gain and signals can be combined with the same phase, the noise figure is improved by 6 dB. The activation of the second receiver boosts the signal level by 3 dB and an additional improvement of almost 3 dB comes from the coherence gain. It was not possible to simultaneously measure more receiver paths using conductive measurements because of the limited number of laboratory power splitters and cables. Thus, the OTA measurement was used to measure the noise figure of the full array. The noise figure based on the curve-fitting method matches the radio system level calculations. A single point EVM measurement would yield a noise figure result for the full eight receiver array that was too optimistic.

VI. Link-Budget with Measured Parameters

In this section, we analyze the radio link budget shown in Table 3 with realistic radio performance values from previous sections. It was shown that noise figure of the 1 × 8 radio receiver is 8.0 dB, which corresponds well with RF system calculations. The noise figure of the full 2 × 8 array receiver should be 3 dB better than the 1 × 8

Table 5. Conducted and OTA noise figures at 26.5 GHz.

Receiver array path noise figures (dB)				
	RX3	RX6	RX3 + R6	All RX paths on
Conducted MSE EVM curve fitting	20.3	21.3	14.0	N/A
Conducted single 4% point EVM result	20.1	21.3	14.0	N/A
OTA MSE EVM curve fitting	17.2	20.2	14.5	8.0
OTA single 4% point EVM result	17.1	19.3	14.1	6.7

https://doi.org/10.4218/etrij.2017-0231

array noise figure, and the 8.0 dB figure used is a pessimistic value for the full array at row I.

The measured average coherence gain of the receiver over the frequencies is 5.5 dB, which is 3.5 dB lower than the theoretical value for eight receivers. The antenna gain of 16 receivers with measured antenna gain and coherence gain is 20 dBi − 3.5 dB = 16.5 dBi and this is used for row M. The antenna gain of 16 transmitters was measured as 20 dBi and this value is used for row L.

Front-end losses were decreased to 2.0 dB at row N because filtering is located close to the mixer. Transmission power can be adjusted with an attenuator and a conducted power of 30 dBm is used for analysis at row K.

The radio link margin for the measured values is 132.94 dB, which is 3.93 dB lower than the original values. The expected link distance is reduced from 263.6 m to 183.53 m, which is close to the 200-m requirement for a 2.5 Gbps data rate with a 100-MHz wide signal with 64-QAM modulation. However, note that we used a rather pessimistic path loss coefficient of 2.5 in our calculations.

VII. Conclusions

We implemented a mobile backhaul phased array transceiver and an antenna array based on 5G high data-rate requirements. We introduced a new noise figure measurement method based on OTA EVM measurement, which is easier to use than conducted noise figure measurements for antenna array receivers. Measured results obtained using the proposed OTA noise figure measurement method match well with the traditional conducted noise figure measurement results. A radio link analysis based on the measured radio performances of the proof-of-concept transceiver and antenna array, indicates that our system can reach one of the key 5G system requirements of a 2.5-Gpbs average data speed for a range of 200 m.

Acknowledgements

The research leading to these results has received funding from the European Union H2020 5GPPP under grant n. 723247 and supported by the Institute for Information & communications Technology Promotion (IITP) grant funded by the Korea government (MSIP) (No.B0115-16-0001, 5GCHAMPION).

References

[1] F. Boccardi, R.W. Heath, A. Lozano, T.L. Marzetta, and P. Popovski, "Five Disruptive Technology Directions for 5G," *IEEE Commun. Mag.*, vol. 52, no. 2, Feb. 2014, pp. 74–80.

[2] R.J. Weiler, M. Peter, W. Keusgen, K. Sakaguchi, and F. Undi, "Environment Induced Shadowing of Urban Millimeter-Wave Access Links," *IEEE Wirel. Commun. Lett.*, vol. 5, no. 4, Aug. 2016, pp. 440–443.

[3] H. Kim et al., "A 28 GHz CMOS Direct Conversion Transceiver with Packaged Antenna Arrays for 5G Cellular System," In *IEEE Radio Frequency Integr. Circuits Symp.*, Honolulu, HI, USA, June 4–6, 2017, pp. 69–72.

[4] B. Sadhu et al., "A 28 GHz 32-Element Phased-Array Transceiver IC with Concurrent Dual Polarized Beams and 1.4 Degree Beam-Steering Resolution for 5G Communication," In *IEEE Int. Solid-State Circuits Conf.*, San Francisco, CA, USA, Feb. 5–9, 2017, pp. 128–129.

[5] G. Destino et al., "System Analysis and Design of mmW Mobile Backhaul Transceiver at 28 GHz," In *Eur. Conf. Netw. Commun.*, Oulu, Finland, June 12–15, 2017, pp. 1–5.

[6] M. Mueck et al., "5G CHAMPION—Rolling out 5G in 2018," In *IEEE Globecom Workshops*, Washington, DC, USA, Dec. 4–8, 2016, pp. 1–6.

[7] K. Khalaf et al., "A 60 GHz 8-Way Phased Array Front-End with TR Switching and Calibration-Free Beamsteering in 28 nm CMOS," In *Eur. Solid State Conf.*, Leuven, Belgium, Sept. 11–14, 2017, pp. 203–206.

[8] G. Destino et al., "Deliverable D2.2 5GCHAMPION Key Performance Indicator and Use-Cases Defined and Specification Document Written," 5GCHAMPION Project, 2017, Accessed Sept. 21, 2017. http://www.5g-champion.eu/Documents/5GCHAMPION_D2.2_Final.pdf

[9] E.C. Strinati et al., "Deliverable D1.2 First Period Report," 5GCHAMPION Project, 2017, Accessed Sept. 21, 2017. http://www.5g-champion.eu/Documents/5GCHAMPION_D1.2_Final.pdf

[10] W. Tavernier et al., "Deliverable D2.1 5GCHAMPION Architecture, API, and Interface Document," 5GCHAMPION Project, 2017, Accessed Sept 21, 2017. http://www.5g-champion.eu/Documents/5GCHAMPION_D2.1_Final.pdf

[11] Qorvo, "27.5 – 31 GHz 9 W GaN Power Amplifier," TGA 2595 Data Sheet, Rev. A, 2014.

[12] Z. Xiao, T. He, P. Xia, and X.G. Xia, "Hierarchical Codebook Design for Beamforming Training in Millimeter-Wave Communication," *IEEE Trans. Wirel. Commun.*, vol. 15, no. 5, May 2016, pp. 3380–3392.

[13] J.J. Lee, "G/T and Noise Figure of Active Antennas," *IEEE Trans. Antennas Propag.*, vol. 41, no. 2, Feb. 1993, pp. 241–244.

[14] A. Natarajan et al., "A Fully-Integrated 16-Element Phased-Array Receiver in SiGe BiCMOS for 60-GHz

Communications," *IEEE Solid State J.*, vol. 46, no. 5, May 2011, pp. 1059–1075.
[15] National Instruments, "Modulation Error Ratio (MER) and Error Vector Magnitude (EVM)," 3652EN, 2014.
[16] Keysight, "What is the Relationship between the Error Vector Magnitude and the Signal to Noise Ratio for a 64-QAM signal?" 2012, Accessed Sept. 21, 2017. http://www.keysight.com/main/editorial.jspx?ckey=847674&id=847674&nid=-11143.0.00&lc=eng&cc=UG

Marko E. Leinonen received his MSc and Licentiate in Technology degrees in electrical engineering from the University of Oulu, Finland, in 1996 and 2002, respectively. From 1994 to 2012 he was with Nokia Mobile Phones, Oulu, Finland, working in various positions with radio engineering and technology management. From 2006 to 2007, he was a senior engineering manager in Bangalore, India. From 2012 to 2016, he was a master developer with Ericsson, Oulu, Finland. Since 2017, he has been with the Centre for Wireless Communications, University of Oulu, Finland, where he is currently a project manager. His research interests include wireless radio systems and quality topics in radio engineering. He holds more than 30 granted international patent families concentrating on radio engineering.

Giuseppe Destino received his DrSc degree from the University of Oulu in 2012, and his MSc (EE) degrees simultaneously from the Politecnico di Torino, Italy and University of Nice, France in 2005. Currently, he is working as an Academy of Finland postdoctoral researcher as well as project manager of national and international projects at the Centre for Wireless Communications, University of Oulu, Finland. His research interests include wireless communications, millimeter wave radio access technologies, especially algorithms for channel estimation, hybrid beamforming, and positioning. He has served as a member of the technical program committee of IEEE conferences.

Olli Kursu received his MSc and DrSc degrees in electrical and electronics engineering from the University of Oulu, Finland, in 2006 and 2015, respectively. Currently, he is working as a postdoctoral researcher at the Centre for Wireless Communications, University of Oulu. His research interests include mmW, RF, analog, and mixed signal circuit design for wireless communication systems.

Marko Sonkki received his MSc in electrical engineering from the Department of Electrical and Information Engineering. University of Oulu, Finland, in 2004. In 2013, he received his DrSc in radio telecommunications engineering from the University of Oulu. The topic of his dissertation was wideband and multi-element antennas for wireless applications focusing on antenna design based on spherical and characteristic modes theories. He is currently a post-doctoral researcher with the Centre for Wireless Communications, University of Oulu. His current research interests include the design and analysis of wideband antennas, wideband multimode and full-duplex antennas, MIMO and diversity systems, and antenna array design, including millimeter waves. He is also a deputy manager at the University of Oulu Research Institute Japan – CWC Nippon, and a visiting researcher at the Universitat Politècnica de València, Valencia, Spain.

Aarno Pärssinen received his MSc, Licentiate in Technology, and DrSc degrees in electrical engineering from the Helsinki University of Technology, Finland, in 1995, 1997, and 2000, respectively. From 1994 to 2000, he was with the Electronic Circuit Design Laboratory, Helsinki University of Technology working on direct conversion receivers and subsampling mixers for wireless communications. From 2000 to 2011, he was with the Nokia Research Center, Helsinki, Finland. From 2011 to 2013, he was at Renesas Mobile Corporation, Helsinki, Finland working as a distinguished researcher and RF research manager. From October 2013 to September 2014, he was an associate technical director at Broadcom, Helsinki, Finland. Since September 2014, he has been with the Centre for Wireless Communications, University of Oulu, Oulu, Finland, where he is currently a professor. His research interests include wireless systems and transceiver architectures for wireless communications with special emphasis on RF and analog integrated circuit and system design. He has authored and co-authored one book, one chapter of a book, more than 50 international journal and conference papers. He also holds several patents.

https://doi.org/10.4218/etrij.2017-0231